Supplement of Atmos. Chem. Phys., 25, 4035–4052, 2025
https://doi.org/10.5194/acp-25-4035-2025-supplement


Atmospheric Chemistry and Physics
Open Access

*Supplement of*

# A data-efficient deep transfer learning framework for methane super-emitter detection in oil and gas fields using the Sentinel-2 satellite

**Shutao Zhao et al.**

*Correspondence to:* Yuzhong Zhang (zhangyuzhong@westlake.edu.cn)

## S1. Methane emission signal (ΔR) retrieval

Similar to (Ehret et al. 2022; Irakulis-Loitxate et al. 2022), we derived ΔR by comparing the ratio of band12 and band11 with a reference background without enhanced methane concentrations. The reference background is predicted by multivariate linear regression (MLR) models by pixel. For that, a sliding time window of T (60) dates was set and the patches in the time continuum were extracted (Ehret et al. 2022). To obtain optimal training set of MLR, we firstly introduced an image structural similarity index measure (SSIM) algorithm (Zhou et al. 2004) to discard the n (15) images that were most dissimilar to the date of interest t in the time series. Most of the discarded images contained opaque or circus clouds as shown in Fig. S1. SSIM estimated image distances considering the combination of structure, contrast, and luminance in band11. Band11 is ideal for comparison as it belongs to SWIR range like band12 but the methane absorption is much weaker to present anomalous absorption signal. Then, the proposed LRAD algorithm was deployed to detect and mask the potential artifacts in the SSIM-optimized data continuum. Within the data cube, patches of the past T-n-1 dates were employed to train MLR model and generate band11 and 12 references. If the coefficient of determination ($R^2$) of the MLR was lower than 0.5, the date of interest t was skipped and the S2L1C data was classified as cloudy observations. The calculation formular of ΔR is shown as follows:

$$\Delta R = \frac{band_{12}^{t}/band_{12}^{ref}}{band_{11}^{t}/band_{11}^{ref}} \quad (S1)$$

Considering that band12 exhibits a significantly higher methane absorption capacity compared to band11, any pronounced methane emission event would lead to a noticeable reduction in the pixel values within the ΔR range of 0-1. Consequently, we applied a threshold range of [0, 1] to ΔR in order to mask anomalies and then a threshold of the 5th percentile value was applied to ΔR in order to remove background. In the end, we applied a colormap to map the unitless ΔR matrix into RGB imagery, so the input to the plume detection algorithm conforms to the structure of ResNet50 in order to use ImageNet-based pre-training parameters, and also can provide more hierarchical features to avoid potential accuracy degradation (Shorten and Khoshgoftaar 2019).

## S2. Emission flux quantification and uncertainty estimation

Emission flux rates (Q, kg $h^{-1}$) are calculated for each detected plume-containing ΔR image. Firstly, we employed the radiative transfer model by (Varon et al. 2021) to convert unitless ΔR to methane column enhancements (mol $m^{-2}$). Secondly, we manually defined a plume mask based on the enhancement image. Background enhancement (mean enhancement outside the mask) is subtracted for pixels in the mask. Finally, the emission flux rate Q is computed using the integrated mass enhancement (IME) method (Frankenberg et al. 2016; Varon et al. 2018):

$$Q = \frac{IME \times U_{eff}}{L} \tag{S2}$$

where IME is computed as the sum of methane mass enhancements within the plume mask. $U_{eff}$ (m $s^{-1}$) is the effective wind speed, which is computed based on the GEOS-FP 1 hour average 10-m wind speed $U_{10}$ following the calibration equation developed in (Varon et al. 2021). L (m) is the plume length which is computed as the square root of the plume area.

To estimate the uncertainty for the emission flux rate, we consider three dominant error terms in Eqs. (S1). The random error of IME, mainly originated from retrieval noise, is estimated as the standard deviation of methane column mass enhancement outside the plume mask (Cusworth et al. 2020). The error of GEOS-FP $U_{10}$ is assumed to be 50%, consistent with the ~1.5 m $s^{-1}$ standard deviation given by (Varon et al. 2020). Following (Sánchez-García et al. 2022), an error of 0.01 is assumed for both the slope and intercept of the $U_{eff}$ calibration function. We add the above errors in quadrature to derive the total uncertainty (1σ) of the emission flux.

## S3. Labeling decision rule of ΔR imagery

We categorized the ΔR images into two classes, plume-containing and plume-free, following the procedure in Fig. 5. The determination is mainly based on visual inspection of ΔR images. We first look for the presence of methane plumes in ΔR images. If present, we then examine whether the potential methane plume signal is roughly aligned with wind direction and is free from surface and cloud interference. We use Goddard Earth Observing System-Fast Processing (GEOS-FP) 10 m wind reanalysis data as main information of wind direction (Varon et al. 2020). Since we find that the wind direction in the GEOS-FP 10-m wind data often does not align with the plume direction, the difference between plume and wind direction tolerated by this labeling process is less than 90°. Nonetheless, there are still a few cases where the plume morphology is distinct but the difference in wind direction is greater than 90°. To this end, the visual inspection of plume is supplemented by directions of nearby smoke plumes (if available) seen in RGB images. Subsequently, we use SWIR and RGB images to rule out potential interference by surface and cloud. It is noted that artifacts originate from low reflectivity surface features, so we focus on the least reflective pixels in the SWIR images. If the "plume" morphology in ΔR image presents to be the low-reflectivity region in SWIR images, then we discriminate it as a false signal.

## S4. Synthetic dataset generation

We collected the ΔR backgrounds from cloud-free Sentinel-2 L1C data in 2023, following the methane signal retrieval process outlined in Fig. 1. Then, the backgrounds were combined with the simulated methane plumes (source rate: 15000kg/h, five different plume shapes, generated by (Gorroño et al. 2023)), using the methodology described in (Jongaramrungruang et al. 2022) and Radman et al. 2023. This approach ensures that the six synthetic datasets share the same plume characteristics but feature different and diverse background noises. Fig. S13 shows examples of the synthetic plume-containing images, which closely resemble the real ones in Fig. 7, both exhibiting relatively strong background noises. For fair comparison, all six synthetic test sets have the same parameters, consisting of 34 images each (10 plume-containing, 24 plume-free).

## Figures

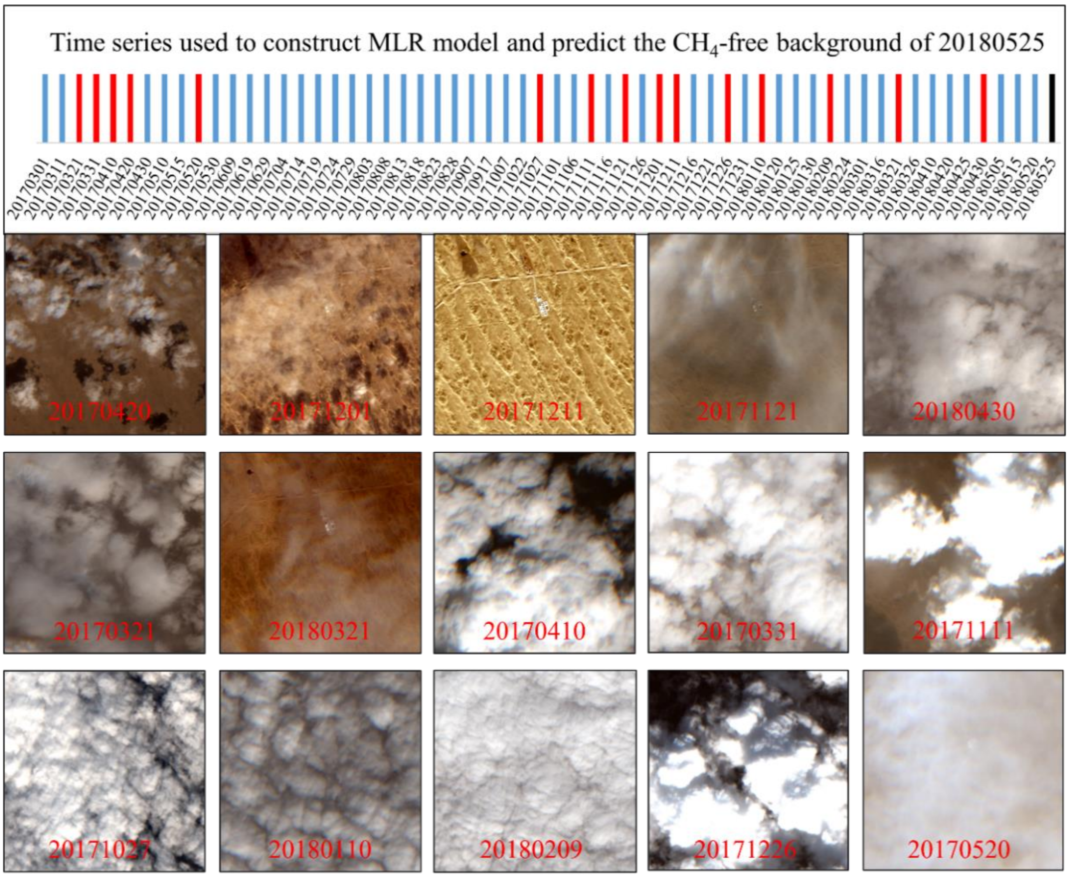


**Fig. S1.** RGB images of the S2L1C observations discarded by SSIM (take 20180525 as an example)

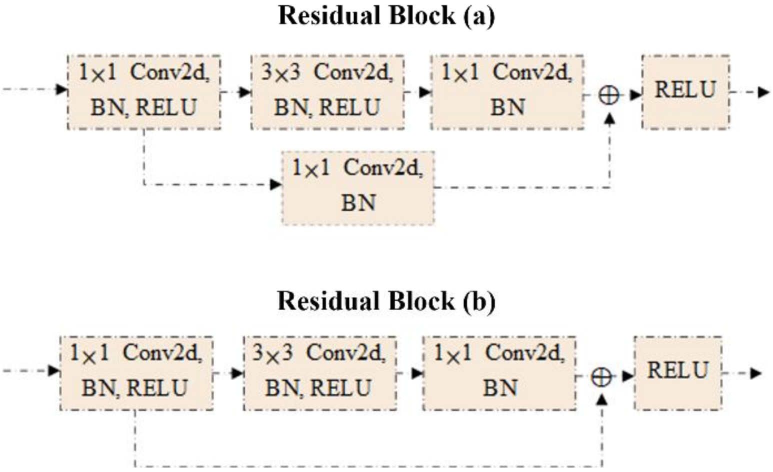


**Fig. S2.** Architecture of residual blocks in DSAN.

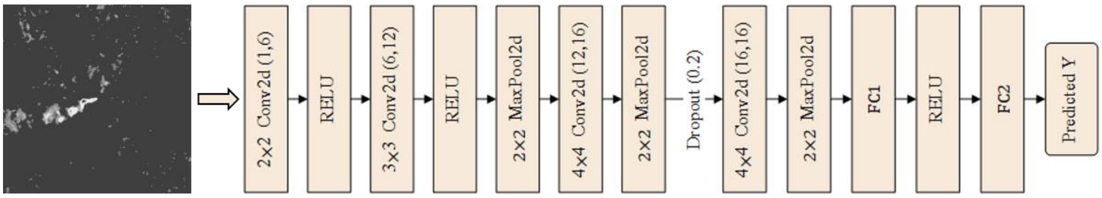


**Fig. S3.** Architecture of MethaNet proposed by (Jongaramrungruang et al. 2022).

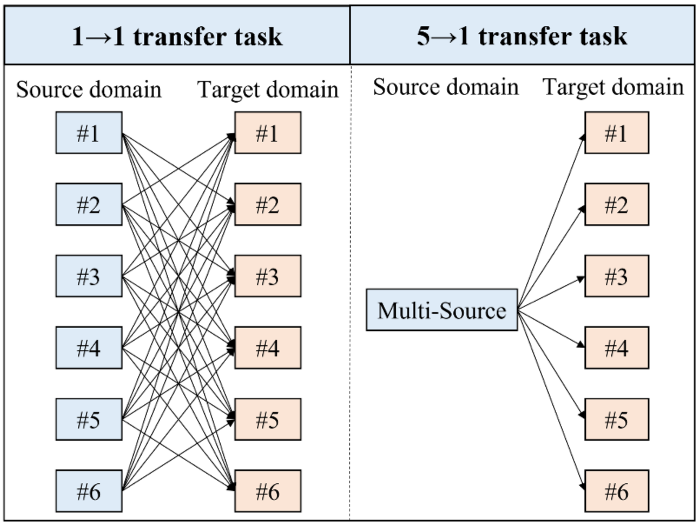


**Fig. S4.** Models were trained and assessed on two kinds of transfer tasks. "1→1": single source domain to single-target domain and "5→1": multi-source domain to single-target domain (multi-source domain is a fusion of all the datasets except for the target dataset).

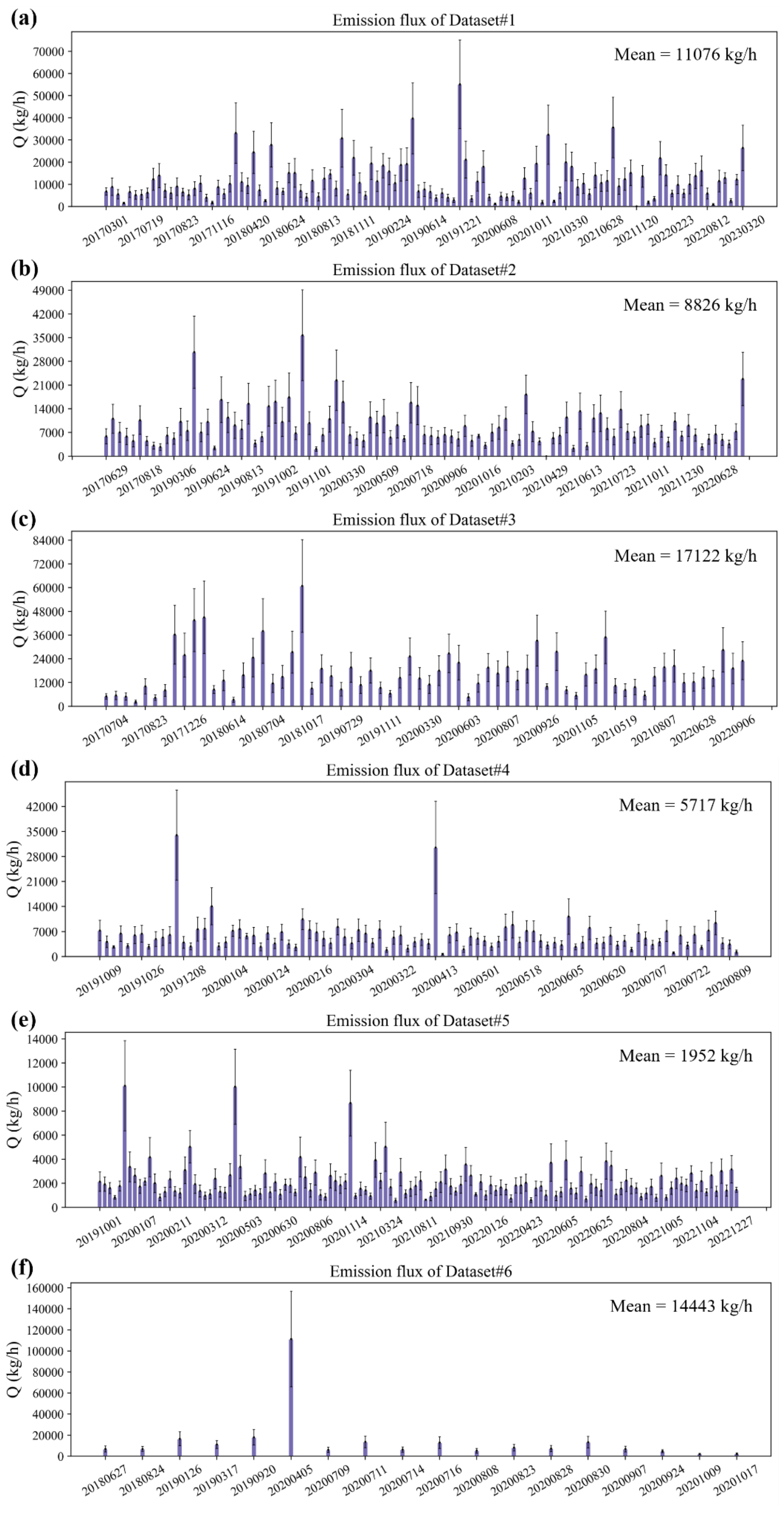


**Fig. S5.** Emission flux (kg/h) and uncertainty quantification of the methane plumes in Dataset#1-6

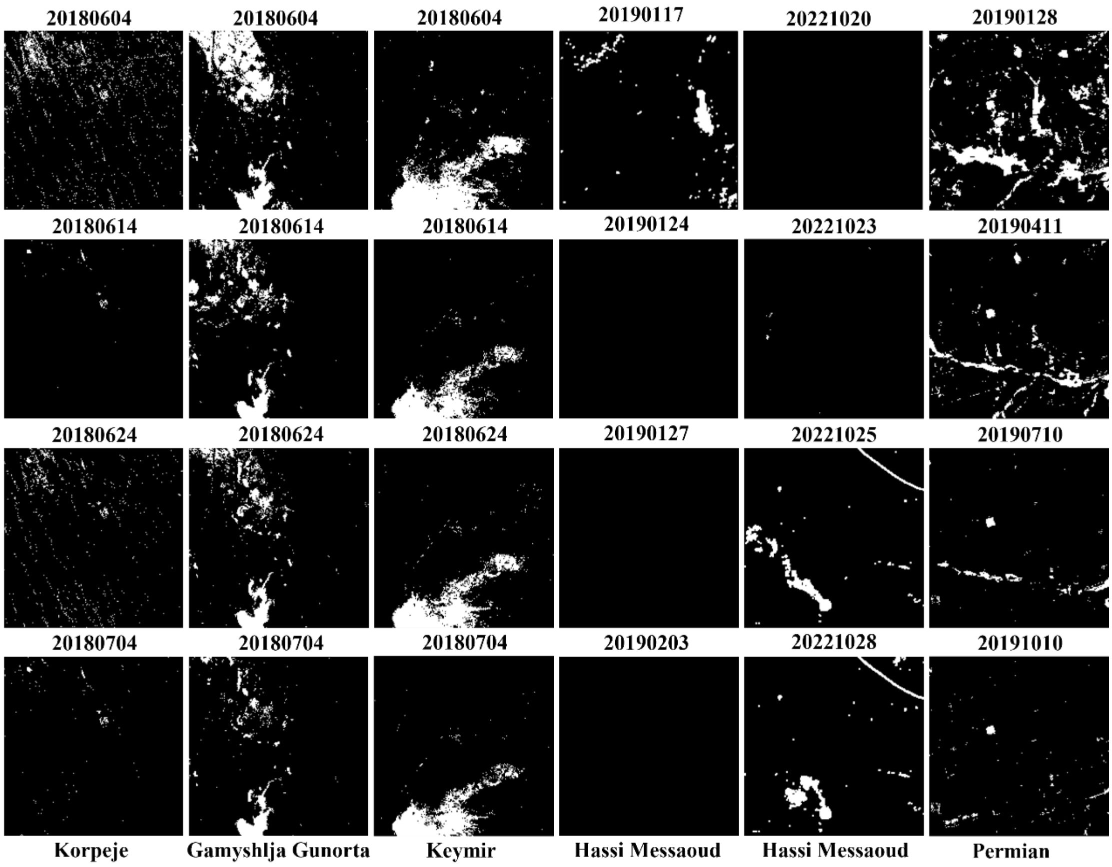


**Fig. S6.** Examples of the adaptive denoising masks over the six methane point sources generated by the LRAD algorithm. White color represents pixels that are filtered out as artifacts.

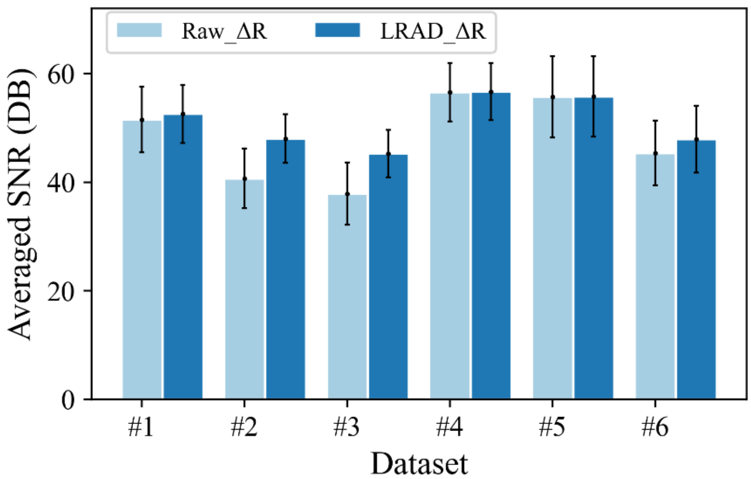


**Fig. S7.** Comparison of the averaged signal-to-noise ratios (SNRs) of the six ΔR datasets before and after deploying the LRAD algorithm.

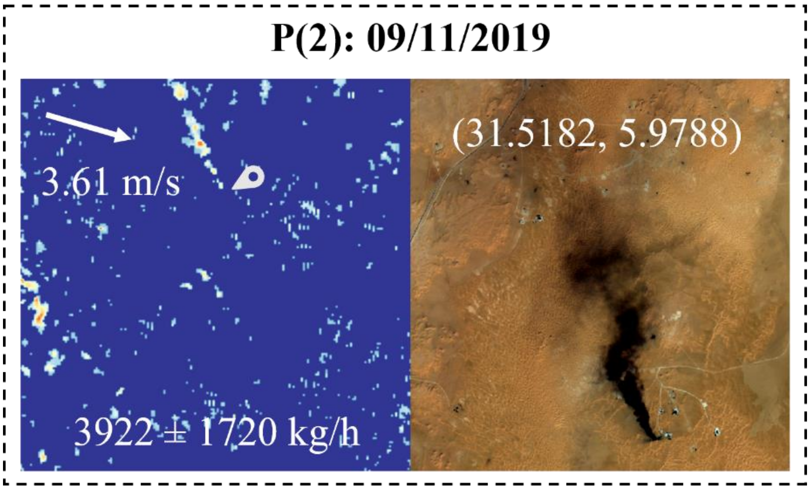


**Fig. S8.** False negative detection in source P(2), and the corresponding RGB images extracted from Sentinel-2 L1C product.

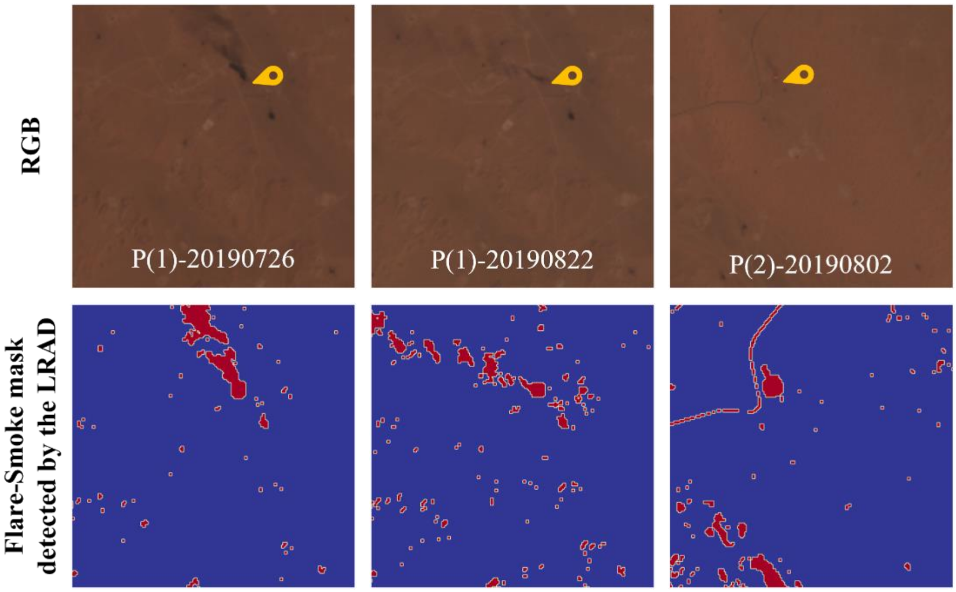


**Fig. S9.** Top row shows RGB images of flaring at P(1) and P(2), which are extracted from Sentinel-2 L1C product. Bottom row presents the flare and smoke (red pixels) masks detected by the LRAD algorithm. Yellow pins indicate the locations of flaring facilities.

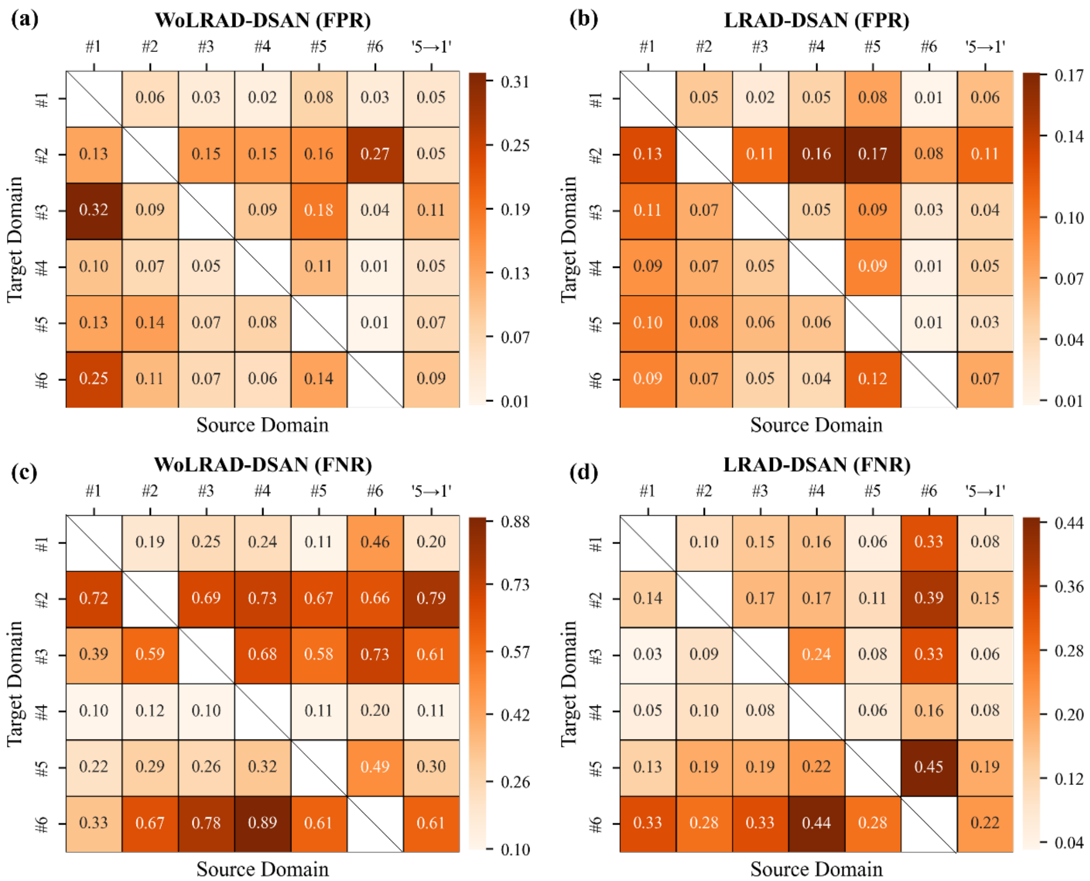


**Fig. S10.** False positive rate (FPR, FP/(FP + TN)) and false negative rate (FNR, FN/(FN + TP)) on the transfer tasks given by the WoLRAD-DSAN model and the LRAD-DSAN model. Each square represents a transfer task. '5→1' indicates that the source domain is fused from five datasets excluding the target domain dataset. Note that the WoLRAD-DSAN refers to the DSAN framework applied to datasets without incorporating the LRAD denoising mask.

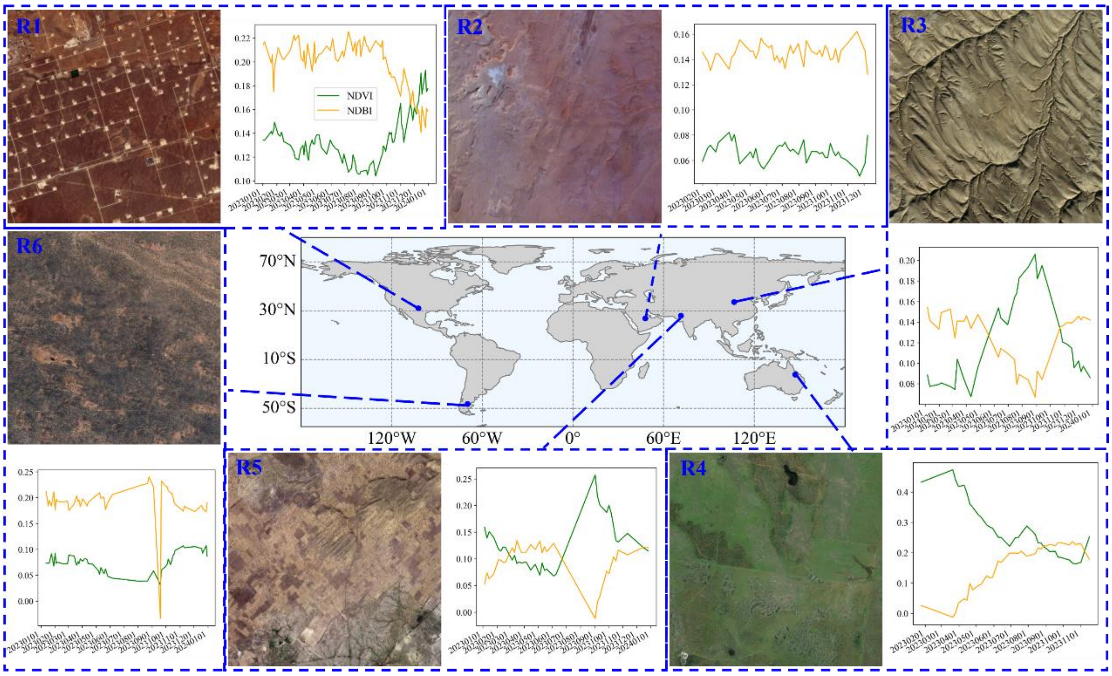


**Fig. S11.** RGB images of the six regions used to generate the synthetic test sets, along with the averaged NDVI-NDBI variation curves for 2023. NDVI and NDBI can serve as proxies for surface conditions to some extent.

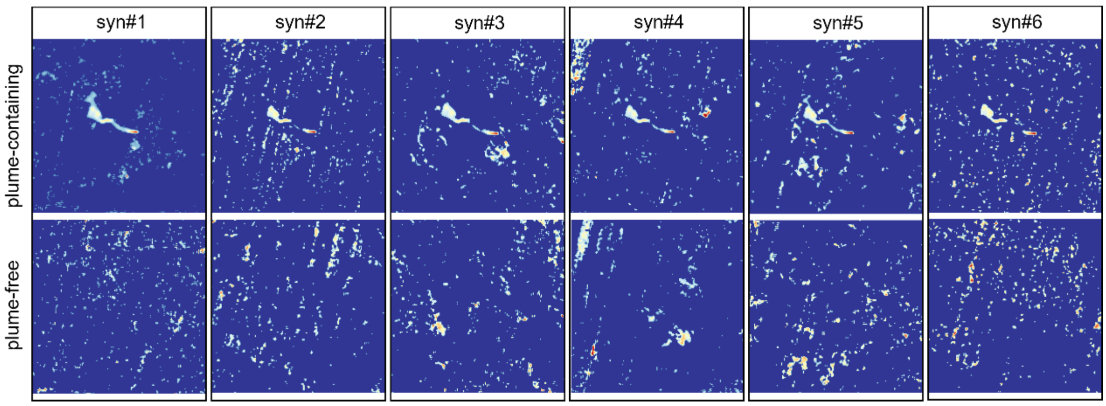


**Fig. S12.** Examples of the plume-containing and plume-free images in ΔR datasets Syn#1- Syn #6.

## Tables

**Table S1** Training, validation, and test sets separation for different types of models and tasks.

| Model | Task | Training set | Validation set | Test set |
|---|---|---|---|---|
| MethaNet, ResNet-50, VGG16, EfficientNet-V2L | ‘1→1’ | $80\% Dataset\#x_i$ [a] | $20\% Dataset\#x_i$ | $Dataset\#x_j$ [b] |
| | ‘5→1’ | $80\% \sum_{i=1}^{n=5} Dataset\#x_i$ | $20\% \sum_{i=1}^{n=5} Dataset\#x_i$ | $Dataset\#x_j$ |
| DSAN | ‘1→1’, | $Dataset\#x_i$ | *n/a* | $Dataset\#x_j$ |
| | ‘5→1’ | $\sum_{i=1}^{n=5} Dataset\#x_i$ | *n/a* | $Dataset\#x_j$ |
| | application for new source detection | $\sum_{i=1}^{n=6} Dataset\#x_i$ | *n/a* | *3537 ΔR images* |

[a-b] $Dataset\#x_i$ and $Dataset\#x_j$ refer to one of the Dataset#1~#6 as listed in Table 3. Here, $i \neq j$, meaning that the source and target datasets in each task are distinct, ensuring no overlap between them.

**Table S2** Performances of MethaNet, ResNet-50, and DSAN models on test sets of the ‘1→1’ transfer tasks.

| Task # | Class | MethaNet | | | ResNet-50 | | | DSAN | | |
|---|---|---|---|---|---|---|---|---|---|---|
| | | Precision | Recall | Accuracy | Precision | Recall | Accuracy | Precision | Recall | Accuracy |
| 1-2 | contain | 0.74 | 0.55 | 0.76 | 0.70 | 0.80 | 0.80 | 0.80 | 0.86 | 0.87 |
| | free | 0.77 | 0.89 | | 0.87 | 0.80 | | 0.92 | 0.87 | |
| 1-3 | contain | 0.85 | 0.59 | 0.87 | 0.64 | 0.89 | 0.84 | 0.76 | 0.97 | 0.91 |
| | free | 0.87 | 0.96 | | 0.96 | 0.83 | | 0.99 | 0.89 | |
| 1-4 | contain | 0.78 | 0.71 | 0.86 | 0.71 | 0.92 | 0.87 | 0.81 | 0.95 | 0.92 |
| | free | 0.89 | 0.92 | | 0.97 | 0.85 | | 0.98 | 0.91 | |
| 1-5 | contain | 0.76 | 0.20 | 0.65 | 0.78 | 0.78 | 0.81 | 0.86 | 0.87 | 0.89 |
| | free | 0.64 | 0.96 | | 0.84 | 0.84 | | 0.90 | 0.90 | |
| 1-6 | contain | 0.36 | 0.50 | 0.90 | 0.19 | 0.71 | 0.77 | 0.36 | 0.67 | 0.89 |
| | free | 0.96 | 0.93 | | 0.97 | 0.77 | | 0.97 | 0.91 | |
| 2-1 | contain | 0.74 | 0.84 | 0.80 | 0.80 | 0.82 | 0.83 | 0.93 | 0.90 | 0.93 |
| | free | 0.86 | 0.76 | | 0.85 | 0.83 | | 0.92 | 0.95 | |
| 2-3 | contain | 0.78 | 0.59 | 0.85 | 0.57 | 0.92 | 0.80 | 0.82 | 0.91 | 0.92 |
| | free | 0.87 | 0.94 | | 0.97 | 0.75 | | 0.97 | 0.93 | |
| 2-4 | contain | 0.87 | 0.73 | 0.89 | 0.77 | 0.92 | 0.90 | 0.84 | 0.90 | 0.92 |
| | free | 0.90 | 0.96 | | 0.97 | 0.89 | | 0.96 | 0.93 | |
| 2-5 | contain | 0.86 | 0.15 | 0.65 | 0.80 | 0.80 | 0.83 | 0.88 | 0.81 | 0.87 |
| | free | 0.63 | 0.98 | | 0.85 | 0.85 | | 0.87 | 0.92 | |

| | | | | | | | | | | |
|---|---|---|---|---|---|---|---|---|---|---|
| 2-6 | contain | 0.38 | 0.28 | 0.91 | 0.18 | 0.71 | 0.75 | 0.45 | 0.72 | 0.91 |
| | free | 0.94 | 0.96 | | 0.97 | 0.76 | | 0.98 | 0.93 | |
| 3-1 | contain | 0.87 | 0.77 | 0.84 | 0.82 | 0.91 | 0.87 | 0.97 | 0.85 | 0.92 |
| | free | 0.83 | 0.90 | | 0.92 | 0.83 | | 0.89 | 0.98 | |
| 3-2 | contain | 0.84 | 0.57 | 0.80 | 0.68 | 0.79 | 0.79 | 0.81 | 0.83 | 0.87 |
| | free | 0.79 | 0.94 | | 0.87 | 0.79 | | 0.90 | 0.89 | |
| 3-4 | contain | 0.94 | 0.64 | 0.88 | 0.63 | 0.92 | 0.83 | 0.88 | 0.92 | 0.94 |
| | free | 0.87 | 0.98 | | 0.96 | 0.79 | | 0.97 | 0.95 | |
| 3-5 | contain | 0.77 | 0.30 | 0.68 | 0.77 | 0.76 | 0.81 | 0.91 | 0.81 | 0.88 |
| | free | 0.66 | 0.94 | | 0.83 | 0.84 | | 0.87 | 0.94 | |
| 3-6 | contain | 0.45 | 0.56 | 0.92 | 0.24 | 0.76 | 0.81 | 0.55 | 0.67 | 0.93 |
| | free | 0.96 | 0.95 | | 0.98 | 0.81 | | 0.97 | 0.95 | |
| 4-1 | contain | 0.85 | 0.78 | 0.84 | 0.87 | 0.94 | 0.91 | 0.94 | 0.84 | 0.90 |
| | free | 0.83 | 0.89 | | 0.94 | 0.89 | | 0.88 | 0.95 | |
| 4-2 | contain | 0.55 | 0.84 | 0.69 | 0.68 | 0.76 | 0.78 | 0.75 | 0.83 | 0.83 |
| | free | 0.87 | 0.60 | | 0.85 | 0.79 | | 0.90 | 0.84 | |
| 4-3 | contain | 0.66 | 0.73 | 0.83 | 0.68 | 0.85 | 0.86 | 0.85 | 0.76 | 0.90 |
| | free | 0.90 | 0.87 | | 0.94 | 0.86 | | 0.92 | 0.95 | |
| 4-5 | contain | 0.64 | 0.22 | 0.62 | 0.83 | 0.72 | 0.82 | 0.91 | 0.78 | 0.88 |
| | free | 0.62 | 0.91 | | 0.82 | 0.89 | | 0.86 | 0.94 | |
| 4-6 | contain | 0.33 | 0.44 | 0.89 | 0.21 | 0.71 | 0.79 | 0.53 | 0.56 | 0.93 |
| | free | 0.95 | 0.93 | | 0.97 | 0.80 | | 0.96 | 0.96 | |
| 5-1 | contain | 0.64 | 0.81 | 0.71 | 0.85 | 0.92 | 0.89 | 0.91 | 0.94 | 0.93 |
| | free | 0.80 | 0.63 | | 0.93 | 0.86 | | 0.95 | 0.92 | |
| 5-2 | contain | 0.49 | 0.79 | 0.63 | 0.62 | 0.84 | 0.76 | 0.75 | 0.89 | 0.85 |
| | free | 0.81 | 0.53 | | 0.89 | 0.71 | | 0.93 | 0.83 | |
| 5-3 | contain | 0.53 | 0.70 | 0.76 | 0.62 | 0.94 | 0.83 | 0.79 | 0.92 | 0.92 |
| | free | 0.88 | 0.78 | | 0.97 | 0.80 | | 0.97 | 0.91 | |
| 5-4 | contain | 0.48 | 0.84 | 0.70 | 0.73 | 0.90 | 0.88 | 0.80 | 0.94 | 0.91 |
| | free | 0.91 | 0.64 | | 0.96 | 0.87 | | 0.97 | 0.91 | |
| 5-6 | contain | 0.17 | 0.61 | 0.75 | 0.29 | 0.82 | 0.85 | 0.33 | 0.72 | 0.87 |
| | free | 0.96 | 0.76 | | 0.98 | 0.85 | | 0.98 | 0.88 | |
| 6-1 | contain | 0.88 | 0.53 | 0.76 | 0.88 | 0.56 | 0.77 | 0.99 | 0.67 | 0.85 |
| | free | 0.71 | 0.94 | | 0.73 | 0.94 | | 0.79 | 0.99 | |
| 6-2 | contain | 0.52 | 0.53 | 0.64 | 0.73 | 0.40 | 0.73 | 0.82 | 0.61 | 0.81 |
| | free | 0.72 | 0.71 | | 0.73 | 0.91 | | 0.80 | 0.92 | |
| 6-3 | contain | 0.84 | 0.24 | 0.79 | 0.75 | 0.37 | 0.80 | 0.90 | 0.67 | 0.89 |
| | free | 0.79 | 0.98 | | 0.81 | 0.96 | | 0.89 | 0.97 | |
| 6-4 | contain | 0.94 | 0.34 | 0.81 | 0.90 | 0.65 | 0.88 | 0.96 | 0.84 | 0.94 |
| | free | 0.79 | 0.99 | | 0.88 | 0.97 | | 0.94 | 0.99 | |
| 6-5 | contain | 0.96 | 0.18 | 0.67 | 0.90 | 0.48 | 0.76 | 0.97 | 0.55 | 0.81 |
| | free | 0.64 | 0.99 | | 0.72 | 0.96 | | 0.75 | 0.99 | |

**Table S3** Performances of VGG16 and EfficientNet-V2L models on test sets of the ‘1→1’ transfer tasks.

| Task# | Class | VGG16 | | | EfficientNet-V2L | | |
|---|---|---|---|---|---|---|---|
| | | Precision | Recall | Accuracy | Precision | Recall | Accuracy |
| 1-2 | contain | 0.88 | 0.38 | 0.75 | 0.77 | 0.62 | 0.79 |
| | free | 0.73 | 0.97 | | 0.80 | 0.90 | |
| 1-3 | contain | 0.94 | 0.52 | 0.87 | 0.82 | 0.63 | 0.87 |
| | free | 0.86 | 0.99 | | 0.88 | 0.95 | |
| 1-4 | contain | 0.88 | 0.62 | 0.87 | 0.86 | 0.79 | 0.90 |
| | free | 0.86 | 0.97 | | 0.92 | 0.95 | |
| 1-5 | contain | 0.97 | 0.28 | 0.70 | 0.86 | 0.42 | 0.73 |
| | free | 0.66 | 0.99 | | 0.70 | 0.95 | |
| 1-6 | contain | 0.40 | 0.24 | 0.92 | 0.40 | 0.56 | 0.90 |
| | free | 0.94 | 0.97 | | 0.96 | 0.93 | |
| 2-1 | contain | 0.99 | 0.61 | 0.82 | 0.88 | 0.83 | 0.87 |
| | free | 0.76 | 0.99 | | 0.86 | 0.91 | |
| 2-3 | contain | 0.95 | 0.57 | 0.88 | 0.69 | 0.70 | 0.84 |
| | free | 0.87 | 0.99 | | 0.89 | 0.89 | |
| 2-4 | contain | 0.96 | 0.53 | 0.86 | 0.84 | 0.82 | 0.91 |
| | free | 0.84 | 0.99 | | 0.93 | 0.94 | |
| 2-5 | contain | 0.94 | 0.38 | 0.73 | 0.90 | 0.61 | 0.81 |
| | free | 0.69 | 0.98 | | 0.77 | 0.95 | |
| 2-6 | contain | 0.43 | 0.33 | 0.92 | 0.33 | 0.67 | 0.87 |
| | free | 0.95 | 0.96 | | 0.97 | 0.89 | |
| 3-1 | contain | 0.95 | 0.84 | 0.91 | 0.96 | 0.82 | 0.90 |
| | free | 0.88 | 0.96 | | 0.86 | 0.97 | |
| 3-2 | contain | 0.75 | 0.76 | 0.82 | 0.79 | 0.64 | 0.81 |
| | free | 0.86 | 0.85 | | 0.81 | 0.90 | |
| 3-4 | contain | 0.88 | 0.85 | 0.92 | 0.89 | 0.83 | 0.92 |
| | free | 0.94 | 0.95 | | 0.93 | 0.96 | |
| 3-5 | contain | 0.92 | 0.55 | 0.80 | 0.91 | 0.57 | 0.80 |
| | free | 0.75 | 0.97 | | 0.76 | 0.96 | |
| 3-6 | contain | 0.38 | 0.50 | 0.90 | 0.41 | 0.50 | 0.91 |
| | free | 0.96 | 0.93 | | 0.96 | 0.94 | |
| 4-1 | contain | 0.94 | 0.77 | 0.88 | 0.94 | 0.81 | 0.89 |
| | free | 0.84 | 0.96 | | 0.86 | 0.95 | |
| 4-2 | contain | 0.75 | 0.61 | 0.78 | 0.74 | 0.58 | 0.77 |
| | free | 0.80 | 0.88 | | 0.78 | 0.88 | |
| 4-3 | contain | 0.79 | 0.67 | 0.86 | 0.83 | 0.67 | 0.88 |
| | free | 0.89 | 0.94 | | 0.89 | 0.95 | |
| 4-5 | contain | 0.91 | 0.54 | 0.79 | 0.89 | 0.55 | 0.79 |
| | free | 0.75 | 0.96 | | 0.75 | 0.95 | |
| 4-6 | contain | 0.46 | 0.67 | 0.92 | 0.50 | 0.61 | 0.92 |

| | | | | | | | |
|---|---|---|---|---|---|---|---|
| | free | 0.97 | 0.94 | | 0.97 | 0.95 | |
| 5-1 | contain | 0.72 | 0.95 | 0.81 | 0.82 | 0.87 | 0.86 |
| | free | 0.95 | 0.70 | | 0.89 | 0.85 | |
| 5-2 | contain | 0.51 | 0.87 | 0.65 | 0.72 | 0.67 | 0.78 |
| | free | 0.88 | 0.52 | | 0.82 | 0.85 | |
| 5-3 | contain | 0.54 | 0.88 | 0.78 | 0.73 | 0.80 | 0.87 |
| | free | 0.95 | 0.74 | | 0.93 | 0.89 | |
| 5-4 | contain | 0.66 | 0.89 | 0.84 | 0.76 | 0.88 | 0.89 |
| | free | 0.95 | 0.82 | | 0.95 | 0.89 | |
| 5-6 | contain | 0.25 | 0.83 | 0.80 | 0.31 | 0.61 | 0.87 |
| | free | 0.98 | 0.80 | | 0.97 | 0.89 | |
| 6-1 | contain | 1.00 | 0.31 | 0.69 | 0.86 | 0.52 | 0.75 |
| | free | 0.64 | 1.00 | | 0.70 | 0.93 | |
| 6-2 | contain | 1.00 | 0.11 | 0.67 | 0.74 | 0.33 | 0.71 |
| | free | 0.66 | 1.00 | | 0.70 | 0.93 | |
| 6-3 | contain | 0.91 | 0.15 | 0.77 | 0.75 | 0.27 | 0.78 |
| | free | 0.77 | 0.99 | | 0.79 | 0.97 | |
| 6-4 | contain | 0.94 | 0.34 | 0.81 | 0.89 | 0.62 | 0.87 |
| | free | 0.79 | 0.99 | | 0.87 | 0.97 | |
| 6-5 | contain | 1.00 | 0.11 | 0.63 | 0.98 | 0.41 | 0.75 |
| | free | 0.62 | 1.00 | | 0.70 | 0.99 | |

**Table S4** Performances of the MethaNet and ResNet-50 on test sets (20%) on validation sets of the non-transfer tasks.

| Dataset# | Class | MethaNet | | | ResNet-50 | | |
|---|---|---|---|---|---|---|---|
| | | Precision | Recall | Accuracy | Precision | Recall | Accuracy |
| 1 | contain | 0.80 | 0.95 | 0.88 | 0.97 | 1.00 | 0.99 |
| | free | 0.96 | 0.82 | | 1.00 | 0.98 | |
| 2 | contain | 0.76 | 0.72 | 0.83 | 0.85 | 1.00 | 0.94 |
| | free | 0.86 | 0.88 | | 1.00 | 0.90 | |
| 3 | contain | 1.00 | 0.67 | 0.90 | 0.83 | 0.95 | 0.93 |
| | free | 0.88 | 1.00 | | 0.98 | 0.93 | |
| 4 | contain | 0.95 | 0.87 | 0.94 | 0.90 | 1.00 | 0.97 |
| | free | 0.93 | 0.98 | | 1.00 | 0.96 | |
| 5 | contain | 0.81 | 0.75 | 0.81 | 0.95 | 0.92 | 0.95 |
| | free | 0.81 | 0.85 | | 0.95 | 0.96 | |
| 6 | contain | 1.00 | 0.80 | 0.98 | 0.83 | 1.00 | 0.99 |
| | free | 0.98 | 1.00 | | 1.00 | 0.99 | |

**Table S5** Performances of the VGG16 and EfficientNet-V2L on test sets (20%) on validation sets of the non-transfer tasks.

| Dataset# | Class | VGG16 | EfficientNet-V2L |
|---|---|---|---|

| | | Precision | Recall | Accuracy | Precision | Recall | Accuracy |
|---|---|---|---|---|---|---|---|
| 1 | contain | 0.93 | 0.64 | 0.81 | 0.88 | 0.67 | 0.81 |
| | free | 0.76 | 0.96 | | 0.78 | 0.93 | |
| 2 | contain | 0.88 | 0.35 | 0.73 | 0.70 | 0.80 | 0.78 |
| | free | 0.70 | 0.97 | | 0.86 | 0.77 | |
| 3 | contain | 0.79 | 0.79 | 0.88 | 0.60 | 0.64 | 0.78 |
| | free | 0.92 | 0.92 | | 0.86 | 0.83 | |
| 4 | contain | 0.94 | 0.84 | 0.94 | 0.94 | 0.89 | 0.95 |
| | free | 0.94 | 0.98 | | 0.96 | 0.98 | |
| 5 | contain | 0.66 | 0.90 | 0.80 | 0.64 | 0.73 | 0.75 |
| | free | 0.94 | 0.75 | | 0.83 | 0.77 | |
| 6 | contain | 1.00 | 0.25 | 0.94 | 1.00 | 1.00 | 1.00 |
| | free | 0.93 | 1.00 | | 1.00 | 1.00 | |

**Table S6** Performances of MethaNet, ResNet-50, and DSAN models on test sets of the '5→1' transfer tasks.

| Task# | Class | MethaNet | | | ResNet-50 | | | DSAN | | |
|---|---|---|---|---|---|---|---|---|---|---|
| | | Precision | Recall | Accuracy | Precision | Recall | Accuracy | Precision | Recall | Accuracy |
| 1 | contain | 0.79 | 0.87 | 0.84 | 0.83 | 0.93 | 0.88 | 0.93 | 0.92 | 0.93 |
| | free | 0.89 | 0.81 | | 0.93 | 0.84 | | 0.93 | 0.94 | |
| 2 | contain | 0.79 | 0.68 | 0.82 | 0.72 | 0.83 | 0.82 | 0.82 | 0.85 | 0.88 |
| | free | 0.83 | 0.90 | | 0.89 | 0.81 | | 0.91 | 0.89 | |
| 3 | contain | 0.84 | 0.71 | 0.89 | 0.68 | 0.83 | 0.85 | 0.89 | 0.94 | 0.95 |
| | free | 0.90 | 0.95 | | 0.94 | 0.86 | | 0.98 | 0.96 | |
| 4 | contain | 0.89 | 0.85 | 0.93 | 0.80 | 0.96 | 0.92 | 0.89 | 0.92 | 0.94 |
| | free | 0.94 | 0.96 | | 0.98 | 0.91 | | 0.97 | 0.95 | |
| 5 | contain | 0.74 | 0.15 | 0.62 | 0.86 | 0.74 | 0.84 | 0.95 | 0.81 | 0.90 |
| | free | 0.61 | 0.96 | | 0.83 | 0.92 | | 0.87 | 0.97 | |
| 6 | contain | 0.35 | 0.50 | 0.89 | 0.22 | 0.71 | 0.80 | 0.47 | 0.78 | 0.92 |
| | free | 0.96 | 0.92 | | 0.97 | 0.81 | | 0.98 | 0.93 | |

**Table S7** Performances of VGG16 and EfficientNet-V2L models on test sets of the '5→1' transfer tasks.

| Task# | Class | VGG16 | | | EfficientNet-V2L | | |
|---|---|---|---|---|---|---|---|
| | | Precision | Recall | Accuracy | Precision | Recall | Accuracy |
| 1 | contain | 0.92 | 0.81 | 0.88 | 0.88 | 0.89 | 0.90 |
| | free | 0.86 | 0.94 | | 0.91 | 0.90 | |
| 2 | contain | 0.89 | 0.43 | 0.77 | 0.77 | 0.65 | 0.80 |
| | free | 0.75 | 0.97 | | 0.82 | 0.89 | |
| 3 | contain | 0.94 | 0.77 | 0.93 | 0.87 | 0.80 | 0.92 |

| | | | | | | | |
|---|---|---|---|---|---|---|---|
| | free | 0.92 | 0.98 | | 0.93 | 0.96 | |
| 4 | contain | 0.96 | 0.84 | 0.94 | 0.84 | 0.94 | 0.93 |
| | free | 0.94 | 0.99 | | 0.97 | 0.93 | |
| 5 | contain | 0.98 | 0.30 | 0.70 | 0.95 | 0.64 | 0.83 |
| | free | 0.66 | 0.99 | | 0.79 | 0.98 | |
| 6 | contain | 0.47 | 0.78 | 0.92 | 0.38 | 0.72 | 0.89 |
| | free | 0.98 | 0.93 | | 0.98 | 0.90 | |

**Table S8** Details of the six methane-free regions used to generate the synthetic plume datasets.

| Index | Sentinel-2 tile ID | Coordinates (latitude, longitude) [a] | Land Cover [b] | Country |
|---|---|---|---|---|
| Syn#1 | T13SGR | (31.9973°, -102.3284°) | Shrubland | U.S. |
| Syn#2 | T38QQM | (23.7908°, 47.8399°) | Bare areas | Saudi Arabia |
| Syn#3 | T48SXG | (37.1046°, 106.6562°) | Grassland | China |
| Syn#4 | T55KER | ( -22.3304°, 147.0094°) | Mosaic T and shrub (>50%) / herbaceous cover (<50%) | Australia |
| Syn#5 | T42RYP | (25.8768°, 71.4514°) | Mosaic natural vegetation (Tree, shrub, herbaceous cover) (>50%) / cropland (<50%) | India |
| Syn#6 | T19GDJ | (-46.4407°, -69.7106°) | Tree cover, needleleaved, evergreen, closed to open (>15%) | Argentina |

[a] Coordinates are the center of the sampling area.

[b] Land cover type near the emitter is obtained from the annual ESA/CCI land cover map 2020 [https://maps.elie.ucl.ac.be/CCI/viewer/index.php] as a reference. It is noted that the land cover map has a spatial resolution of 300 m, which cannot reflect surface features smaller than an area of 300 $m^2$.

**Table S9** LRAD-DSAN model performances on the six synthetic plume datasets.

| Test set | Class | TP[a] | FP[b] | TN[c] | FN[d] | Precision | Recall | Macro-F1 score | Accuracy |
|---|---|---|---|---|---|---|---|---|---|
| Syn#1 | contain | 7 | 0 | 24 | 3 | 1.00 | 0.89 | 0.88 | 0.91 |
| | free | | | | | 0.70 | 1.00 | | |
| Syn#2 | contain | 8 | 1 | 23 | 2 | 0.89 | 0.92 | 0.89 | 0.91 |
| | free | | | | | 0.80 | 0.96 | | |
| Syn#3 | contain | 10 | 3 | 21 | 0 | 0.77 | 1.00 | 0.90 | 0.91 |
| | free | | | | | 1.00 | 0.88 | | |
| Syn#4 | contain | 8 | 0 | 24 | 2 | 1.00 | 0.92 | 0.92 | 0.94 |
| | free | | | | | 0.80 | 1.00 | | |
| Syn#5 | contain | 8 | 1 | 23 | 2 | 0.89 | 0.92 | 0.89 | 0.91 |
| | free | | | | | 0.80 | 0.96 | | |
| Syn#6 | contain | 7 | 0 | 24 | 3 | 1.00 | 0.89 | 0.88 | 0.91 |
| | free | | | | | 0.70 | 1.00 | | |

[a-d] TP (true positive), FP (false positive), TN (true negative), and FN (false negative) represent specific categories of predictions.

## References


Cusworth, D. H., Duren, R. M., Thorpe, A. K., Tseng, E., Thompson, D., Guha, A., Newman, S., Foster, K. T., and Miller, C. E.: Using remote sensing to detect, validate, and quantify methane emissions from California solid waste operations, Environ. Res. Lett., 15, 054012, https://doi.org/10.1088/1748-9326/ab7b99, 2020.

Ehret, T., De Truchis, A., Mazzolini, M., Morel, J.-M., d'Aspremont, A., Lauvaux, T., Duren, R., Cusworth, D., and Facciolo, G.: Global Tracking and Quantification of Oil and Gas Methane Emissions from Recurrent Sentinel-2 Imagery, Environ. Sci. Technol., 56, 10517–10529, https://doi.org/10.1021/acs.est.1c08575, 2022.

Frankenberg, C., Thorpe, A. K., Thompson, D. R., Hulley, G., Kort, E. A., Vance, N., Borchardt, J., Krings, T., Gerilowski, K., Sweeney, C., Conley, S., Bue, B. D., Aubrey, A. D., Hook, S., and Green, R. O.: Airborne methane remote measurements reveal heavy-tail flux distribution in Four Corners region, Proc. Natl. Acad. Sci. U.S.A., 113, 9734–9739, https://doi.org/10.1073/pnas.1605617113, 2016.

Irakulis-Loitxate, I., Guanter, L., Maasakkers, J. D., Zavala-Araiza, D., and Aben, I.: Satellites detect abatable super-emissions in one of the world's largest methane hotspot regions, Environ. Sci. Technol., 56, 2143–2152, https://doi.org/10.1021/acs.est.1c04873, 2022.

Sánchez-García, E., Gorroño, J., Irakulis-Loitxate, I., Varon, D. J., and Guanter, L.: Mapping methane plumes at very high spatial resolution with the WorldView-3 satellite, Atmos. Meas. Tech., 15, 1657–1674, https://doi.org/10.5194/amt-15-1657-2022, 2022.

Shorten, C., and Khoshgoftaar, T. M.: A survey on Image Data Augmentation for Deep Learning, J. Big Data, 6, 60, https://doi.org/10.1186/s40537-019-0197-0, 2019.

Varon, D. J., Jacob, D. J., Jervis, D., and McKeever, J.: Quantifying time-averaged methane emissions from individual coal mine vents with GHGSat-D satellite observations, Environ. Sci. Technol., 54, 10246–10253, https://doi.org/10.1021/acs.est.0c01213, 2020.

Varon, D. J., Jacob, D. J., McKeever, J., Jervis, D., Durak, B. O. A., Xia, Y., and Huang, Y.: Quantifying methane point sources from fine-scale satellite observations of atmospheric methane plumes, Atmos. Meas. Tech., 11, 5673–5686, https://doi.org/10.5194/amt-11-5673-2018, 2018.

Varon, D. J., Jervis, D., McKeever, J., Spence, I., Gains, D., and Jacob, D. J.: High-frequency monitoring of anomalous methane point sources with multispectral Sentinel-2 satellite observations, Atmos. Meas. Tech., 14, 2771–2785, https://doi.org/10.5194/amt-14-2771-2021, 2021.

Zhou, W., Bovik, A. C., Sheikh, H. R., and Simoncelli, E. P.: Image quality assessment: from error visibility to structural similarity, IEEE Trans. Image Process., 13, 600–612, https://doi.org/10.1109/TIP.2003.819861, 2004.